MATERIALS SCIENCE

The hidden structure dependence of the chemical life of dislocations

X. Zhou[1]*, J. R. Mianroodi[1,2]*, A. Kwiatkowski da Silva[1], T. Koenig[3], G. B. Thompson[3], P. Shanthraj[4], D. Ponge[1], B. Gault[1,5], B. Svendsen[1,2], D. Raabe[1]*

Dislocations are one-dimensional defects in crystals, enabling their deformation, mechanical response, and transport properties. Less well known is their influence on material chemistry. The severe lattice distortion at these defects drives solute segregation to them, resulting in strong, localized spatial variations in chemistry that determine microstructure and material behavior. Recent advances in atomic-scale characterization methods have made it possible to quantitatively resolve defect types and segregation chemistry. As shown here for a Pt-Au model alloy, we observe a wide range of defect-specific solute (Au) decoration patterns of much greater variety and complexity than expected from the Cottrell cloud picture. The solute decoration of the dislocations can be up to half an order of magnitude higher than expected from classical theory, and the differences are determined by their structure, mutual alignment, and distortion field. This opens up pathways to use dislocations for the compositional and structural nanoscale design of advanced materials.

INTRODUCTION

Dislocations play a fundamental role in the mechanical behavior of many materials (*1*, *2*). They often form three-dimensional (3D) networks, with a total length that can reach 1 light-year per cubic meter in metals and semiconductors. Having been studied for nearly a century (*3*, *4*), much is known about their mechanical character and behavior. Much less well characterized, however, is their interaction with, and influence on, the material chemistry. Probing and understanding the interplay between structure and chemistry is essential as it influences many material properties, often by orders of magnitude (*5*, *6*), ranging from catastrophic embrittlement in steels (*7*–*9*) to enhanced phonon scattering in thermoelectrics (*10*, *11*). To fully understand these interactions, one needs atomic-scale resolution, both in experiments (*2*, *6*, *12*–*16*) and modeling/simulation (*1*, *17*–*23*). When studying these phenomena in a Pt-Au model system, we made an unexpected discovery: Unlike the expected cloud-like, quasi-random distribution of solute atoms around dislocations suggested by Cottrell and Bilby (*2*) over 70 years ago, there is no simple solute decoration of dislocation cores. Instead, we find a wide range of decoration states deviating from the bulk composition. More specifically, a wide range of segregation amounts (enrichment factors from 2.9 up to 8.5) has been observed, all higher than the value of 2.2 predicted by classical theory (*24*) for the case of Cottrell segregation to an edge dislocation in Pt-Au. Such a strong dependence of solute segregation behavior on defect type, lying behind their hidden chemical nature, has not previously been elucidated. This is carried out in the current work with the help of atomistic simulations, enabling a systematic study of the effect of defect type on segregation behavior and local solubility. We found that in an otherwise homogeneous solid solution, each defect configuration exhibits its own specific segregation state that deviates, in some cases, by up to one order of magnitude from the bulk composition (see defect segregation levels marked on top of the bulk phase diagram in Fig. 1). These findings show a much stronger influence of defects on the local chemical composition than expected based on theory (*24*). Thus, they have a profound influence on all material properties determined by the interplay of chemistry and defects. In the following, a short summary of methods is presented, followed by a detailed discussion on each of the observed defects and their local chemistry.

RESULTS AND DISCUSSION

We magnetron-sputtered a 1-μm thin-film Pt–7 atomic % (at %) Au sample to form a homogeneous solid-solution alloy. The free-standing samples were heat-treated at 1300 K for 15 min to trigger Au segregation to the defects. Correlative transmission electron microscopy (TEM)–precession electron diffraction (PED) and atom probe tomography (APT) (*25*–*27*) are used for quantitative structural and chemical analyses. Complementary diffusive molecular dynamics (DMD) simulations (*18*–*20*) based on the embedded atom method (EAM) potential for Pt-Au from (*28*) provides further insight into these observations, in particular, into the relations between segregation morphology, defect type, and the defect stress field. See the Supplementary Materials for the details of sample preparation and simulation setup.

In Fig. 1A, linear and disc-like regions (pointed by arrows) indicate lattice imperfections. The gray arrow in Fig. 1A points to a low-angle grain boundary (LAGB) and the other colored arrows to distinct dislocations. Together, the local orientation spread (LOS) map (Fig. 1B) and the atom probe reconstruction (Fig. 1, C and D) determine the identity of these features. The APT data were taken from the region enclosed by the green dashed line in Fig. 1C. APT reconstruction (Fig. 1D) determines the morphology of the regions of segregated Au associated with different defects. APT crystallographic analysis identifies four defect types: (i) dislocation array in a LAGB, (ii) free-standing glissile dislocation, (iii) stacking fault tetrahedron (SFT), and (iv) Frank loop. Figure 1E shows Au at % profiles across these defects in the corresponding colored boxes in

---

[1] Max-Planck-Institut für Eisenforschung, 40237 Düsseldorf, Germany. [2] Material Mechanics, RWTH Aachen University, 52062 Aachen, Germany. [3] Department of Metallurgical and Materials Engineering, The University of Alabama, Tuscaloosa, AL 35401, USA. [4] The Department of Materials, The University of Manchester, M13 9PL Manchester, UK. [5] Department of Materials, Royal School of Mines, Imperial College London, London, UK.

*Corresponding author. Email: x.zhou@mpie.de (X.Z.); j.mianroodi@mpie.de (J.R.M.); d.raabe@mpie.de (D.R.)

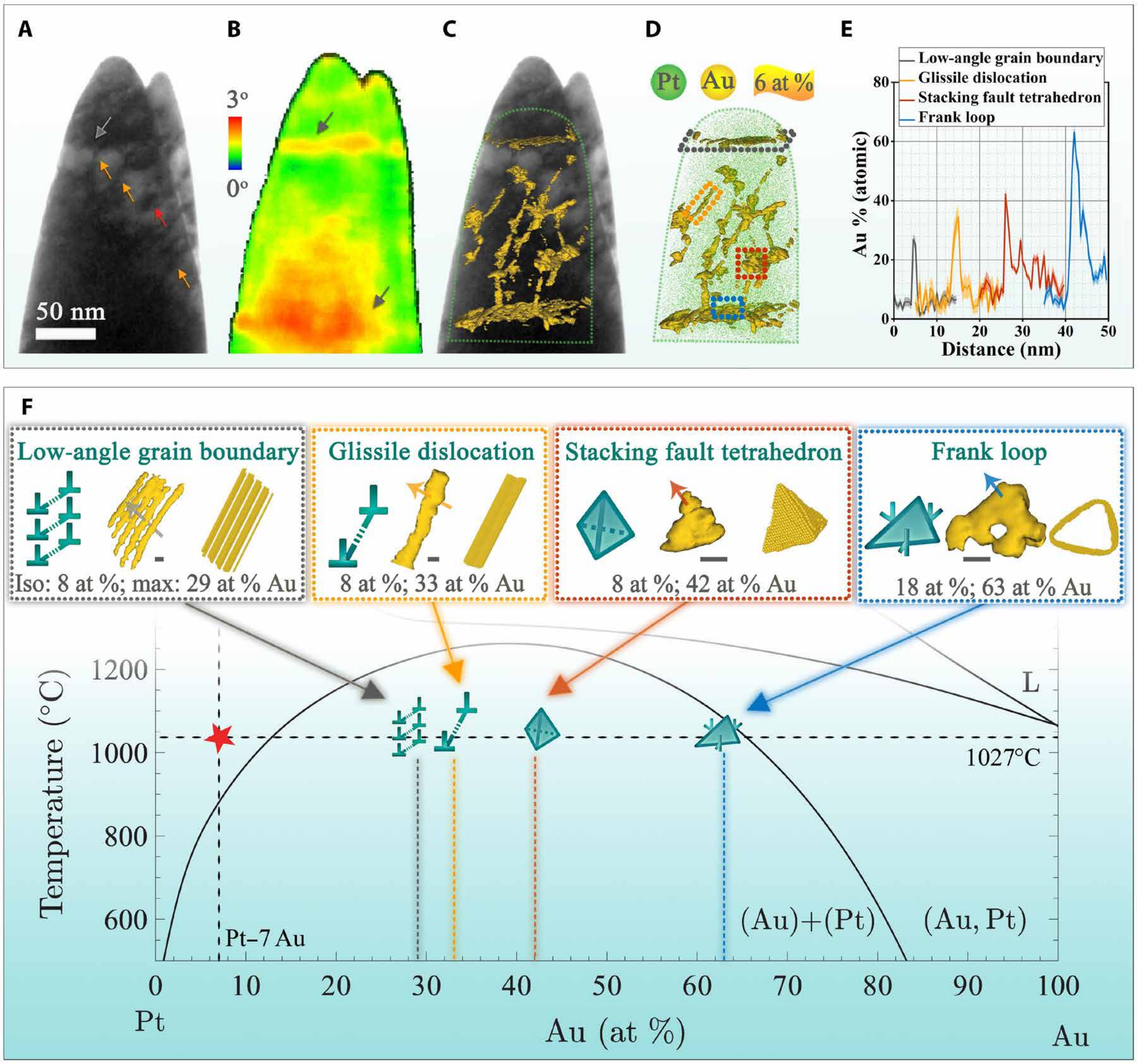

Fig. 1. Cross-correlative study of a Pt–7 at % Au thin film specimen annealed at 1300 K for 15 min. (**A**) TEM-based bright-field image of specimen tip oriented normal to $(\bar{1}1\bar{1})$ crystallographic direction. (**B**) PED-based LOS map. (**C**) APT-based reconstruction of the 6 at % segregated Au isosurface superimposed on the bright-field image from (A). The *x* at % isosurface represents the region (voxels) containing *x* or more at % Au. (**D**) Spatial distribution of Pt (green) and Au (gold) atoms in the specimen tip and the isosurfaces from (C). (**E**) Au at % profiles across particular defects shown in the upper panels in (F). The direction of the profiles in (E) is indicated by the arrows in (F). These include (i) LAGB (gray profile normal to dislocation array), (ii) glissile dislocation (yellow profile parallel to slip plane normal $\vec{n} = [\overline{111}]/\sqrt{3}$), (iii) SFT (red profile parallel to $\vec{n} = [1\bar{1}\bar{1}]/\sqrt{3}$), and (iv) Frank loop (blue profile parallel to $\vec{n} = [1\bar{1}\bar{1}]/\sqrt{3}$). (**F**) Top: Each panel shows an image (middle) of each observed defect type, corresponding defect symbols (left), and a DMD simulation result (right) in the colored boxes. The numbers in each box are the Au at % isosurface (Iso) values for imaging (left) and maximum (max) solute at % near the defects (right). The maximum values are obtained from the Au at % profile in (E). A length of 5 nm is indicated by a gray bar. Bottom: room pressure equilibrium Pt-Au phase diagram. See main text for discussion.

Fig. 1D. Figure 1F (top row) displays a symbol (left), an APT reconstruction (middle), and a DMD simulation result (right) for each defect type. The upper and lower limits of solute segregation to these defects are reported in the Supplementary Materials (fig. S3).

In the binary Pt-Au phase diagram in Fig. 1F (below), the red star marks the bulk alloy composition (vertical line) and temperature (horizontal line) that was used to allow Au segregation and equilibration at the defects. The vertical lines below each defect type indicate the corresponding local Au at %. Au segregation to the defects shown varies from approximately 29 at % for a dislocation array in a LAGB to 63 at % for a Frank loop. This reveals two points: First, the magnitude of the segregation depends strongly on the hosting defect type. Second, it is not only the generic individual structure of the defect that determines the decoration but also its exact topological arrangement, through the associated distortion fields. The diffusion length of Au in Pt is about 1.0 μm (1300 K, 15 min), using $\sqrt{D\tau}$ and a diffusivity of Au in Pt of $D = 1.1 \times 10^{-15}$ m^2/s (*29*). Because this is far above the defect extension and spacing considered here, the Au at % can be regarded as being equilibrated, with steady-state values.

Low-angle grain boundary

As shown in Fig. 1F, Au segregates to parallel linear defects in the LAGB. The low-angle character of the boundary was determined by electron diffraction and confirmed by the pole patterns obtained from the atom probe crystallographic analysis (fig. S4). On the basis of the PED results, the LAGB has a misorientation of 2.5° with a tilt component of 2.4° and a twist component of 0.1°. On the basis of the morphology of the experimental Au segregation region (Fig. 2, B to D) and DMD simulation results (Fig. 2, E and F), the parallel linear defect microstructure in the LAGB is interpreted to represent an array of edge and mixed dislocations, in agreement with classical theory (*24*). More specifically, as shown in Fig. 2A, on the basis of the APT crystallographic analysis, parallel lenticular (cross-sectional view) Au segregation regions (Fig. 2B) lie in the $(11\bar{1})$ plane, a common slip plane family in the face-centered cubic (fcc) system. The dislocation array aligns at 30° to the glide plane normal as shown in Fig. 2C. The quantitative Au at % profiles (Fig. 2D) indicate that the region of segregated Au is about 3 nm wide in the direction normal, and about 8 nm wide in the direction parallel, to the array plane. From the Au at % profile along $\vec{\xi}\,[2\bar{1}1]$ (black) in Fig. 2D, we found that the dislocation in this LAGB has a segregation range of 18 to 29 at % Au. Such variation in segregation level may be due to atomic-scale features such as kinks or jogs along the dislocation lines. We also observed some solute depletion regions, e.g., in profiles normal to the plane of the dislocation array (red) and normal to the dislocation array in the array plane (blue) in Fig. 2D. For instance, the minimum Au content in the red Au % profile is about 5 at % lower than the bulk composition.

To gain further insight, corresponding DMD simulations have been carried out for dislocation arrays consisting of both single-sign and dipole configurations. Because the latter configuration results in segregated Au distributions in better qualitative agreement with the experimental observations, the dislocation dipole array is a more likely configuration for this LAGB. More specifically, the experimental dipole configuration is interpreted as a combination of pure-edge and mixed dislocations (Fig. 2, A, E, and F), resulting in a tilt angle between adjacent grains of $\varphi = b/d = 1.9°$ (*30*). This value is comparable to the experimental value of 2.4°. As shown in Fig. 2E, the stress field of such a dipole results in maximum Au segregation to the regions between each monopole (Fig. 2F) where the hydrostatic stress is positive (note that the lattice constant a_0 of Au is 4% larger than that of Pt). Au depletion (Fig. 2E) occurs in regions with negative hydrostatic stress (Fig. 2F). For better visualization, the range in Fig. 2F is limited to values between 4 and 9 at % Au. The minimum and maximum Au at % values (averaged in voxel units of 0.6^3 nm^3) are 3.1 and 13.6, respectively. Note that the maximum of 13.6 at % Au predicted by DMD is substantially lower than the experimentally observed value of 24 at % Au obtained from a cross section normal to the dislocation line vector $\vec{\xi}\,[2\bar{1}1]$ (Fig. 2C).

One reason for the deviation between experiment and prediction may be the inaccuracy of the EAM potential from (*28*) used in the DMD simulations. In particular, the values of the elastic constants of pure Pt and Au predicted by this potential are smaller than the experimental values, resulting in a lower stress field and less segregation. Besides this, the close spacing of the defects may result in an experimental value for local average Au at %, which is larger (e.g., 9 at % for the same box as DMD around the LAGB) than the 7 at % (i.e., bulk value) assumed in the DMD simulations. In addition, the DMD simulations are carried out at lower and fixed average composition (i.e., rather than fixed chemical potential), which also results in less segregation compared to experiments. Increasing the average Au at % in the simulation indeed results in more segregated Au (e.g., 12.3 at % bulk composition would result in a segregation value of about 24 at % to LAGB). Moreover, we investigated a few possible dislocation configurations in the LAGB and identified one that results in a good qualitative match to the experimentally observed segregation distribution. In real materials, local dislocation

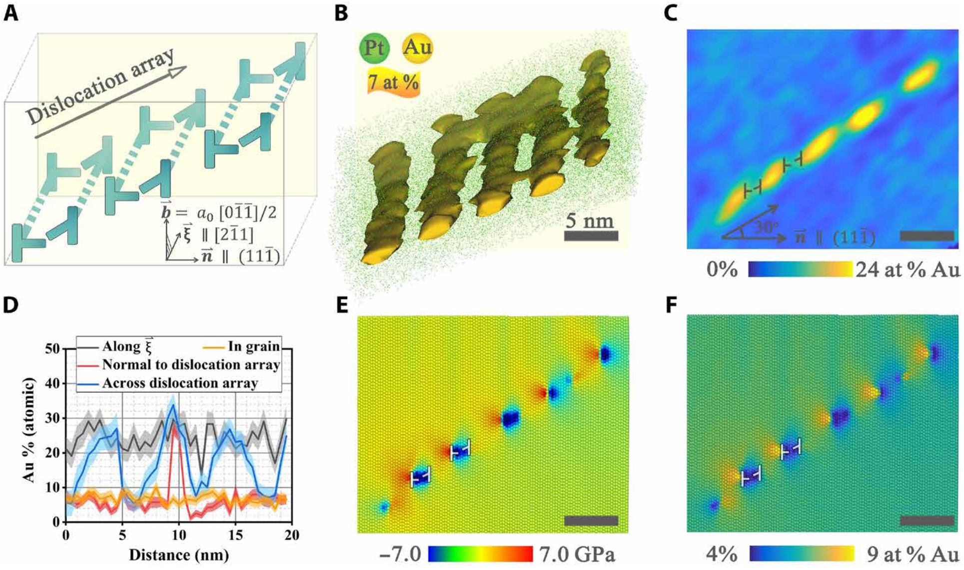

Fig. 2. Analysis of a LAGB with 2.5° misorientation observed in the atom probe specimen tip. (**A**) Model dislocation array for the LAGB. (**B**) APT results for the 7 at % Au isosurface near the LAGB. (**C**) Au at % in cross section normal to dislocation line vector $\vec{\xi}\,[2\bar{1}1]$. (**D**) Au at % profiles along $\vec{\xi}$ (black), normal to the plane of the dislocation array (red), and normal to the dislocation array in the array plane (blue). For comparison, an Au at % profile in defect-free bulk crystal (yellow) is also displayed. (**E**) Atomic virial hydrostatic stress field and (**F**) segregated Au at % for the model dislocation array in (A) predicted by DMD simulation. The gray bars in (B), (C), (E), and (F) indicate a length of 5 nm. Minimum and maximum Au at % values (averaged in voxel units of 0.6^3 nm^3) are 3.1 and 13.6, respectively. Color contouring is cropped for better visualization. Simulation results are also presented for an array of dissociated dislocations in the Supplementary Materials.

configurations can be more complicated. For instance, multiple types of dislocation pairs may be present in a given LAGB, in addition to the geometrically necessary ones. As mentioned above, dislocation lines may also contain jogs and kinks. These details can influence the solute distribution and morphology at defects. Experimental resolution of these, however, is only possible with full 3D atomic-level characterization, in both structure and chemical space. This is not possible for relevant sample volumes with currently available characterization technology. Although APT is the state-of-the-art technique for composition quantification, its current resolving power is near atomic at best (*31*). Besides this, APT characterization depends on a reconstruction technique involving uncertainties such as ion flight path and positioning aberration, related to the exact shape of the electrical field at the atomic surface from which an atom evaporates (*32*). Because of this, fine structures can be therefore slightly blurred (*33*). Further details concerning the APT crystallographic analysis and DMD simulation are summarized in the Supplementary Materials (figs. S4 and S6). Note that, for better comparison with experimental results, the DMD results are presented in voxel-averaged form, using the same voxel size as the one in APT analysis. Raw (nonaveraged) segregation ranges are reported in the Supplementary Materials.

Free-standing, glissile dislocations

These dislocations form and glide in the bulk during the bending and peeling of the film from the substrate (Fig. 3A). As in the LAGB, the morphology of segregated Au regions is lenticular (Fig. 3, B and C), and these regions are interpreted as decorated dislocations (*12*–*16*, *34*–*37*). These dislocations are, for the most part, associated with the $(\bar{1}\bar{1}\bar{1})$ plane (identified in fig. S2). On the basis of the crystallographic analysis and loading configuration, we infer that these (Fig. 3B) are edge dislocations with a $a_0[01\bar{1}]/2$ Burgers vector, consistent with the crystallographic orientation of the specimen tip and bending-based loading in Fig. 3A.

As shown in Fig. 3C, the lenticular distribution of segregated Au around a given decorated dislocation is wider (about 10 nm) in the Burgers vector direction than in the $(\bar{1}\bar{1}\bar{1})$ plane normal direction (about 5 nm). Figure 3D displays Au at % profiles for the dislocation in Fig. 3C along (i) the dislocation line direction ξ (black curve), (ii) the glide plane normal $\vec{n}$ (red curve), and (iii) the direction of the Burgers vector $\vec{b}$ (blue curve). The compositional fluctuations along the dislocation line could be due to, for example, the presence of kinks and jogs. Because the length of these is of the order of a single Burgers vector (about 0.27 nm), these features are most likely super jogs/kinks that can be formed by sequential dislocation cutting events (*17*, *38*).

Figure 3E displays DMD simulation results for Au segregation to a dissociated edge dislocation. Corresponding Au at % profiles along the Burgers vector (blue curve) and normal to the glide plane (red curve) are shown in Fig. 3F. For comparison, the Au at % profile along the Burgers vector of a perfect edge dislocation (violet curve) is also shown. Note that the width of the simulated Au distribution around a dissociated edge dislocation (blue curve, Fig. 3F) is closer to the experimental case (blue curve, Fig. 3D) than that around a perfect edge dislocation (violet curve, Fig. 3F). In contrast to the DMD result of little or no Au segregation to the stacking fault (i.e., Suzuki segregation), however, the experimental results suggest the opposite, i.e., even more Au segregation to the region where the stacking fault would be assuming that the dislocation is dissociated. Interpretation of this dislocation as dissociated is also complicated by the fact that the stacking fault is too narrow to experimentally distinguish between the amount of Au segregating to the partial cores and to the intervening stacking fault.

Sessile dislocations

As shown, for example, in Figs. 1D and 3B, sessile dislocations are mostly located at the junctions of glissile dislocations. These sessile dislocations could be pinning the glissile dislocations and be a reason

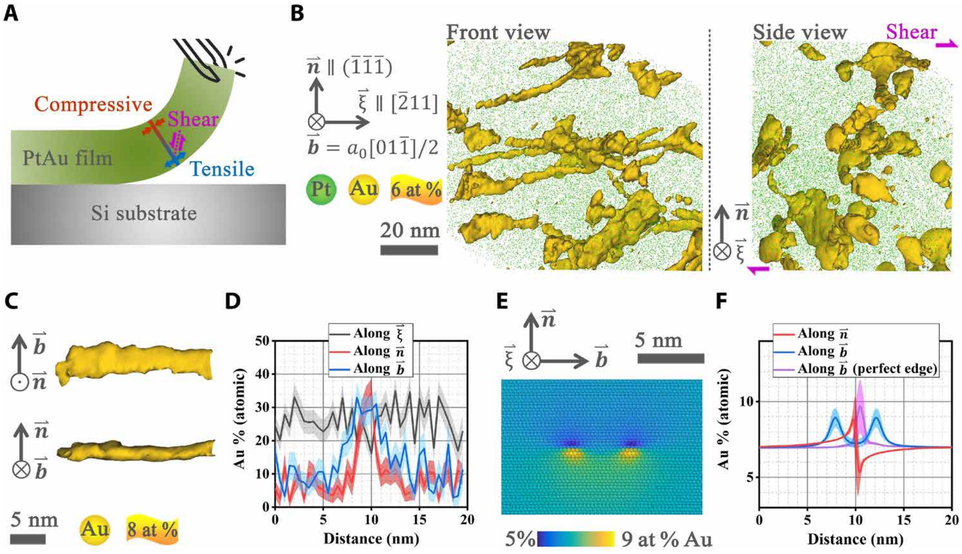

Fig. 3. Analysis of bulk glissile dislocations. (**A**) Sketch of deformation and resulting stress state in the thin film due to peeling from the substrate. (**B**) Front view (normal to $[01\bar{1}]$, left) and side view (normal to $[\bar{2}11]$, right) of a group of decorated dislocations by the 6 at % Au isosurfaces in APT measurement. The most likely Burgers vector is $\vec{b} = a_0[01\bar{1}]/2$. (**C**) Region of segregated Au (8 at % Au isosurfaces) around a glissile dislocation. (**D**) Au at % profiles along (i) the dislocation line vector $\xi = [\bar{2}11]/\sqrt{6}$, (ii) the slip plane normal $\vec{n} = [\bar{1}\bar{1}\bar{1}]/\sqrt{3}$, and (iii) $\vec{b}$, for the dislocation in (C). (**E**) DMD simulation of Au segregation to a dissociated edge dislocation. (**F**) Simulated Au at % profiles along (i) $\vec{n}$ (red curve) and (ii) $\vec{b}$ (blue curve). For comparison, the segregated Au at % profile along $\vec{b}$ of a perfect edge dislocation is also shown.

for the presence of glissile dislocations even after high-temperature annealing. In contrast to the lenticular morphology (Fig. 3, C and D) of the region of segregated Au observed around bulk glissile dislocations, tetrahedral (Fig. 4A, I) and triangular (Fig. 4A, II) morphologies are observed around sessile dislocations in the $(1\bar{1}\bar{1})$ plane. In the following, the former are interpreted as SFTs and the latter as Frank loop. As already documented in Fig. 1E, substantially more Au segregates to these sessile dislocations than to glissile dislocations.

Stacking fault tetrahedron

As shown in Figs. 1E (red curve) and 4B (top), up to 40 at % Au segregates to the center of the SFT in the $(1\bar{1}\bar{1})$ plane. The at % Au profiles normal to the dislocation line directions $\vec{\xi}_i$ in the $(1\bar{1}\bar{1})$ plane shown in Fig. 4B (top) indicate a relatively uniform distribution of segregated Au in these directions. On the other hand, a multilayer segregated Au distribution is indicated by the multiple (at least three) peaks in the at % profile (red curve) in Fig. 1E, which was measured normal to $(1\bar{1}\bar{1})$ plane. Each peak of the profile is interpreted as a layer of segregated Au. As shown, in comparison to the main layer (40 at %), successively less Au segregated to the other layers, which also appear to be of lesser extent (see Au isosurface in red box; Fig. 1F). On the basis of the segregation morphology (Fig. 4A, I), this defect is interpreted as a SFT (*24*, *39*, *40*). SFTs form as a result of Frank loop dissociation. A Frank loop is a stacking fault bounded by three (sessile) Frank partial dislocations of Burgers vector $\vec{b} = a_0\langle 111\rangle/3$. These can form by vacancy condensation during annealing at 1300 K and subsequent cooling. Transformation of these to SFTs proceeds via the Silcox-Hirsch mechanism (*41*). SFTs are often observed in TEM investigations of metals and alloys with low stacking fault energy, for instance, in gold (*41*) and copper (*42*).

To gain further insight, segregation to single sessile dislocations and to defect structures formed by them has been simulated using DMD. Frank partials and stair-rod dislocations are typical sessile dislocations in fcc systems. The DMD results presented in the Supplementary Materials imply that the amount of Au segregation to a straight sessile partial Frank dislocation (fig. S7D) is about three times that to a straight glissile perfect edge dislocation (fig. S7A). Simulation results also indicate that if a Frank loop is sufficiently small, then it will relax to a SFT [as suggested by the Silcox-Hirsch mechanism; (*41*)]. In the case of a SFT (Fig. 4A, III), the DMD results show 53 at % Au segregation to the SFT corners (i.e., to the dislocation intersections). Comparison with the experimental segregate morphology in Fig. 4A (I) suggests that the latter is strongly affected by the local magnification effect (*32*, *33*). In this case, the predicted localization of segregated Au in the SFT corners shown in Fig. 4A (III) is experimentally not resolvable. The Au at % profile in the SFT perpendicular to $\vec{\xi}_2$ shown in Fig. 4C (violet curve) shows two peaks, i.e., 15 at % across $\vec{\xi}_2$ and approximately 50 at %, at the intersection between $\vec{\xi}_1$ and $\vec{\xi}_3$.The central region between the two peaks represents a stacking fault, to which Au also segregates, representing the Suzuki effect (*43*).

Frank loops

In contrast to the 3D tetrahedral morphology of the region occupied by Au segregation in Fig. 4A (I), the decoration feature in Fig. 4A (II) has a 2D triangular shape. Corresponding Au at % profiles perpendicular to $\vec{\xi}_1$, $\vec{\xi}_2$, and $\vec{\xi}_3$ are displayed in Fig. 4B (bottom). One defect possibly consistent with such a segregated Au distribution is an extrinsic Frank loop (Fig. 4A, IV). This type of Frank loop is less likely to transform into a SFT than the (smaller) intrinsic Frank loop. This is investigated in more detail in the Supplementary Materials (fig. S9). In addition, as evident in Fig. 4 [A (II) and B], the Au segregation is not uniform. This asymmetrically segregated Au distribution could be due to, for example, interaction with surrounding dislocations. Note that the Frank loop is quite close to other dislocations in Fig. 1D (blue box). Another possibility could be the inclination of the intersection plane relative to the symmetry of the decoration feature. If the cutting plane [in Fig. 4A (II)] is slightly

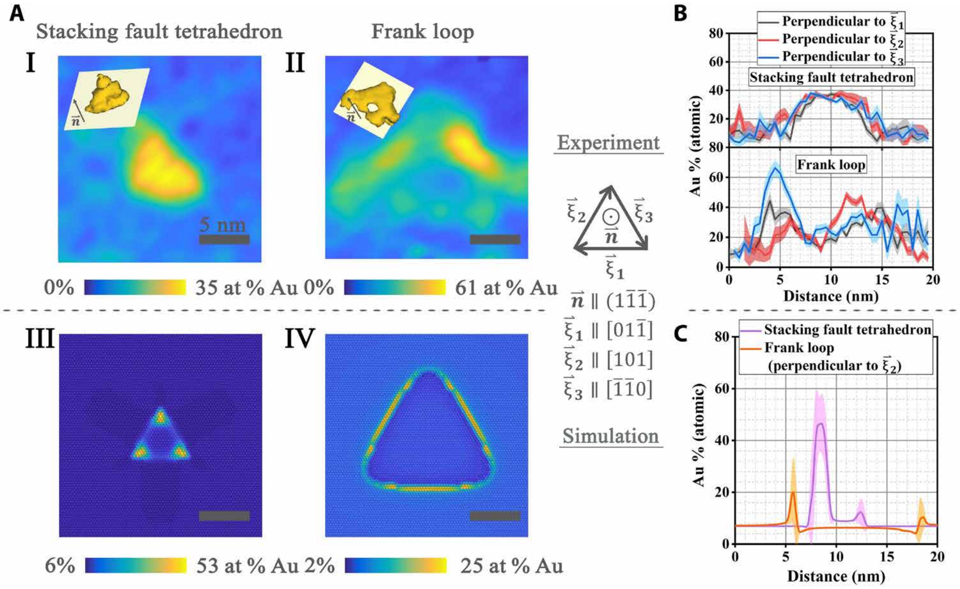

Fig. 4. Analysis of bulk sessile dislocations. (**A**) Tetrahedral (I) and triangular (II) morphologies of the segregated Au region around sessile defects from APT measurements compared with DMD simulations of segregation to a SFT (III) and to a (extrinsic) Frank loop (IV). The insets in I and II display 3D 8 and 18 at.% Au isosurfaces, respectively. The gray bars in I to IV indicate a length of 5 nm. (**B**) APT results for segregated Au at % profiles perpendicular to the line directions $\vec{\xi}_1$, $\vec{\xi}_2$, and $\vec{\xi}_3$. (**C**) DMD results for segregated Au at % profiles perpendicular to $\vec{\xi}_2$. See main text for details.

tilted with respect to the (111) lattice direction, or the defect is slightly rotated, then the observed segregation profile will appear asymmetric (fig. S10).

The current experimental and simulation results indicate that, generally speaking, more segregation takes place to sessile than to glissile dislocations. As discussed in more detail in the Supplementary Materials (fig. S7), this is the case even when there is no corresponding difference in the magnitude of the (positive) hydrostatic stress. For example, despite having a shorter Burgers vector (and thus a lower hydrostatic stress) than a perfect edge glide dislocation (fig. S7 A and D), more Au segregates to each Frank partial in the loop (Fig. 4B, bottom). This means that additional factors besides the magnitude of the (positive hydrostatic) stress influence the level of segregation. For instance, it is known from modeling (*23*) based on microscopic phase-field chemomechanics (MPFCM) that the dependence of the elastic stiffness and intrinsic stacking fault (ISF) energy on solute concentration induces additional driving forces for segregation (fig. S8). As shown by the results in fig. S8 in the Supplementary Materials, DMD simulations based on the Pt-Au EAM potential do include these additional driving forces. Whereas the former is independent of defect type, the latter is not if the defect type involves stacking faults (e.g., dissociated glide dislocations or SFTs). Solute driving forces induced by the dependence of the dislocation core energy on solute concentration are also defect specific. In contrast to modeling based on MPFCM, however, it is unfortunately not possible with DMD to individually determine each of these forces and compare them for different defect types.

Selected additional atom probe observations

Interpretation of characterization results for Au segregation to defects in terms of specific defect types is complicated, in general, by the fact that errors in the determination of atom trajectory from the specimen tip to the detector result in "blurred" or "fuzzy" APT reconstructions of solute distribution around defects, representing the so-called local magnification effect (*32*, *33*). This is even more severe for defects with more complex structure and small volumetric extent such as SFTs (Fig. 4A, I). With this in mind, one can nevertheless interpret further features in the APT dataset. For example, the features observed in Fig. 5 are interpreted in terms of cross-slip, super kinks/jogs, extended node, and dislocation-LAGB interaction, following the treatment of these features in (*24*). On this basis, Fig. 5A is interpreted as a cross-slipped screw dislocation. Note that the ISF energy of Pt is about 130 mJ/m^2, resulting in narrower stacking faults and increased cross-slip probability. On the basis of APT crystallographic analysis (e.g., fig. S4), the two screw dislocations lie in $(11\bar{1})$ and $(\bar{1}\bar{1}\bar{1})$. Dissociation of a perfect screw into two mixed partials results in a hydrostatic core stress field driving solute segregation. Recombination of the partials into a perfect screw for cross-slip results in less Au segregation at the intersection between the glide and cross-slip planes (Fig. 5A).

Changes in dislocation line direction are observed in Fig. 5 (B and C). Depending on whether the slip plane is changed, they are classified into super kinks (no change of glide plane) or super jogs (change of glide plane). Only multiple kinks or jogs can be observed experimentally. Figure 5D displays three dislocations meeting at a junction/extended node. The last example (Fig. 5E) exhibits bulk dislocation interaction with a LAGB having a misorientation angle of 5.2°, a tilt rotation angle of 4.6°, and a twist angle of 2.3°. The dislocation glides in different slip planes before intersecting the LAGB. A segregation level as high as 46 at % Au has been observed in the interaction region. These more complicated cases are the subject of an ongoing investigation to be reported on in the future.

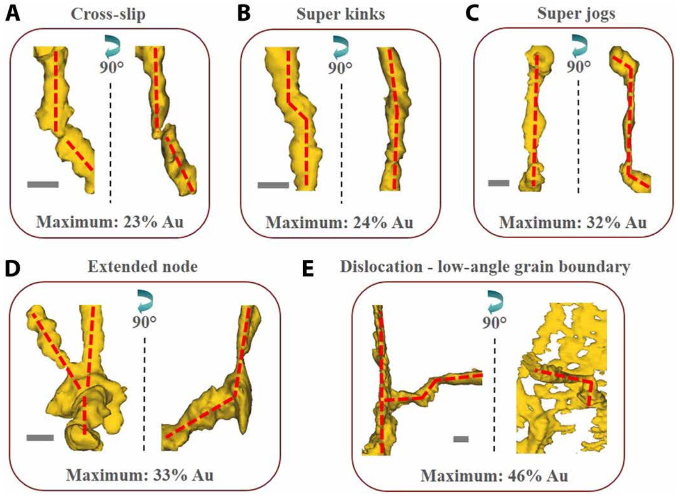

Fig. 5. Dislocation reaction and interactions observed in the atom probe specimen. Examples of (**A**) cross-slip, (**B**) super kinks, (**C**) super jogs, (**D**) extended node, and (**E**) dislocation LAGB interaction indicated by the APT data. A length scale of 5 nm is indicated by a gray bar. In each figure, the right-hand image is rotated 90° to the left relative to the left image.

Table 1 provides the minimum and maximum solute composition values for multiple defect types obtained from Au at % profiles. The values in Table 1 show the most representative values measured at each particular defect type. For example, solute segregation to a LAGB is apparently enhanced (1.6 times) when this boundary is intersected by a glissile dislocation. Glissile dislocations with a lenticular shape have a slightly higher solute level than those with a circular shape. The solute level at the cross-slip junction is 26% lower than those observed for the adjacent glissile dislocations. A SFT intersected by a glissile dislocation contains 1.3 times more segregated solute. These observations imply that interaction among defects also influences solute segregation. Therefore, the structural character for each dislocation investigated has to be specified, supporting our general conclusion that the chemical nature of dislocations is strongly linked to their underlying structure and associated distortion fields. This is also the subject of current and ongoing investigations.

The influence of segregated solute at dislocations on material properties

The Pt-Au alloy being investigated here is an almost ideal model system for conducting joint experimental and theoretical studies on the interplay between solutes and dislocations, in particular related to the structure of the latter. The ideality of this alloy is, in particular, due to its wide mutual solubility range and to the large region of spinodal decomposition in its bulk phase diagram. Beyond its basic relevance as a model alloy system, it also has potential commercial relevance. For instance, the ultralow wear rate and low electrical resistivity of Pt-Au thin films qualify them as a candidate material for highly stressed electrical contact applications as discussed by Curry *et al.* (*44*). Another interesting application is related to Pt-based electrocatalysis in the oxygen reduction reaction of O_2 to H_2O (*45*). Loss of Pt during dissolution under realistic operation conditions, however, makes application of this material over longer periods of

Table 1. Minimum and maximum solute at % for different defect types obtained from profiles across defects in the APT dataset.

Type of defects		Composition (at %)	
Character	Description	Minimum	Maximum
LAGB	Isolated	2	29
	Intersected with a dislocation	1	46
Glissile dislocation	Lenticular shape	3	33
	Lenticular shape	1	30
	Round shape	5	24
	Round shape	4	29
	Cross-slip (at the junction)	4	23(17)
	Super kinks (at the junction)	3	24(19)
	Super jogs	3	32
SFT	Isolated	5	42
	Isolated	2	45
	Intersected with a dislocation	2	52
Frank loops	Extrinsic	3	63
	Intrinsic	4	57

time questionable (*46*). Our preliminary results suggest that the enrichment of Au at defects can postpone the loss of Pt, thereby enhancing the robustness of the material's catalytic performance.

When taking a broader view at these findings, beyond their immediate relevance for the current model alloy system, the variety and complexity of defect-specific solute decoration phenomena observed here open up ample opportunities in using this knowledge for tuning local chemical-structural defect states for the design of specific properties. A few pioneering studies on this subject exist: For instance, Re enrichment to partial dislocations in Ni-based superalloys improves the creep properties (*16*). Ca-doping at dislocation cores in $YBa_2Cu_3O_{7-\delta}$ yields an enhancement of critical current density for high-temperature superconductor application (*47*). Ag-decorated dislocations in PbTe-based thermoelectric materials enhance the material's thermoelectric performance (*11*). The reported influence of specific defects on material properties can be leveraged by modifying their chemical decoration state. Our joint experimental and theoretical work enables general access to a defect-specific solute decoration approach to materials design.

Combined state-of-the-art material characterization and simulation at the atomic scale has revealed the hidden chemical nature of dislocations and related defects going beyond the classic pictures of Cottrell (*2*) (for dislocations) and Suzuki (*43*) (for stacking faults). Results for a deformed and annealed Pt–7 at % Au model alloy show structure-specific Au segregation to a number of dislocation-based defects. We studied a set of dislocation arrays with increasing complexity, including dislocations in LAGBs, bulk glissile dislocations, and sessile dislocation structures that form SFTs and Frank loops. Au segregation to these defects results in strong, localized spatial variations in chemistry and local compositions at the defects laying well inside the immiscible region of the Pt-Au phase diagram, while the bulk matrix remains in the fully miscible solid solution. Both the characterization results and DMD simulation results show that substantially more Au segregation takes place to SFTs or Frank loops than to free-standing dislocations or to dislocation arrays making up LAGBs. In addition, DMD results for the corresponding defect stress fields imply that this higher affinity of Au to segregate to sessile defects is strongly, but not solely, related to (the magnitude of) the corresponding (positive) hydrostatic stress field. Apparently, other differences (e.g., atomic configuration in the core) are also playing a role for this behavior.

MATERIALS AND METHODS

One-micrometer-thick Pt–7 (at %) Au thin films were prepared from Pt (99.9% purity) and Au (99.9%) elemental targets via magnetron sputtering onto Si substrates in the AJA ATC-1500 system. A base pressure as low as 4×10^{-6} Pa had been reached before sputtering. The substrate was rotated and titled toward the target with a concentric geometry configuration to minimize the composition gradient in the films. The deposition rate was measured as 0.2 nm/s using a quartz crystal at a sputtering power of 75 W for the Pt target and 12 W for Au. The sputtering gas argon was injected into the chamber at a rate of 10 standard cubic centimeters per minute to maintain a pressure of 0.27 Pa. After removal from the chamber, the sputtered Pt–7 (at %) Au film was manually peeled off from the Si substrate for further heat treatment. The detached films were annealed in an in-house developed annealing tube system, which was turbo-pumped to a pressure below 5×10^{-5} Pa and equipped with a gauge inside the tube to monitor the temperature variation in the specimens. The heat treatment consisted in increasing the temperature at a rate of 1 K/s up to 1300 K, holding the specimen at this temperature for 15 min, and subsequent air cooling of the annealing tube down to room temperature in approximately 3 hours before removing the specimen from the tube.

A focus ion beam (FIB) lift-out technique (*25*, *26*) was used to prepare cross-correlative TEM-APT wedge-shaped samples in an FEI Quanta 3D dual beam FIB–scanning electron microscope. The extracted wedge was rotated 90° from its original orientation via a rotation needle so that the electron beam could be perpendicular to the film surface during TEM observation. Afterward, 2-μm-wide segments were cut from the rotated wedge and mounted onto pre-sharpened Si grid posts in a hummingbird TEM holder. The wedges were FIB-sharpened into needle shape tips, and surface damage was removed via a low-energy clean-up procedure. The whole hummingbird holder was transferred to an FEI Tecnai SupertwinF20 (scanning) transmission electron microscope at 200 keV for bright-field imaging and orientation mapping. A series of diffraction patterns from the Pt–7 (at %) Au tip was collected in the NanoMEGAS platform with a scanning step size of 2 nm. The scan was operated with a 0.3° precession angle to minimize the effect of nonsystematic inelastic scattering (*48*). Data analysis and imaging were carried out using TSL OIM 7 software. LOS, a kernel-based misorientation analysis method, was used to determine local variations in misorientation. LOS is calculated by measuring the deviation between the orientation of each point in a given grain and the average orientation of that grain (*49*, *50*). We used it to visualize crystalline imperfections within the grains or LAGB with a small misorientation angle. In the last step, the Pt–7 (at %) Au tip was moved to a Cameca puck specimen assembly and field-evaporated in Local Electrode Atom Probe 5000 XS operated with a specimen set point of 40 K and a laser pulse energy of 280 pJ at a pulse repetition rate of 200 kHz for a 0.8% atoms per pulse detection rate. The atom probe data were analyzed using the Integrated Visualization and Analysis Software 3.8.4 platform. To avoid reconstruction artifacts, the first 3 million ions were dropped from the two peaks observed at the very end of the tip resulting from the FIB milling process.

A TEM plan-view foil was prepared by the FIB lift-out technique. Similar to APT tip preparation, a rotation needle was used to reorient the extracted wedge so that the electron beam would be perpendicular to the substrate during imaging. Plan-view foils provide a larger field of view of the nanocrystalline film to confirm grain sizes, orientation, and grain boundary structures using the aforementioned NanoMEGAS PED platform. Dislocation structures were confirmed by dark-field imaging of the foil.

There exist several methods to model atomistic scale interaction of defects (e.g., dislocations) with solutes [e.g., (*19*, *20*, *23*, *51*)]. Simulation results presented in this work are based on the DMD formulation from (*19*, *52*) and on an embedded atom potential for Pt-Au (*28*). This potential reproduces the Pt-Au phase diagram relatively well. It has been successfully applied to model Au segregation to grain boundaries (*28*). The DMD formulation used in this work is capable of modeling processes such as dislocation climb, vacancy diffusion, and mass/heat transport (*52*). The corresponding DMD code is available as a module/user package (*52*) in Large-scale Atomic/Molecular Massively Parallel Simulator (LAMMPS) (*53*). Ovito (*54*) was used for postprocessing and visualization. Unless otherwise stated, the simulations were carried out at 1300 K and zero stress until no further change in composition and configuration was observed. The local compositions were obtained via averaging with respect to cubic volumes having a side length of 0.5 nm for comparability with the corresponding atom probe results.

SUPPLEMENTARY MATERIALS

Supplementary material for this article is available at http://advances.sciencemag.org/cgi/content/full/7/16/eabf0563/DC1

REFERENCES AND NOTES

1. V. V. Bulatov, L. L. Hsiung, M. Tang, A. Arsenlis, M. C. Bartelt, W. Cai, J. N. Florando, M. Hiratani, M. Rhee, G. Hommes, T. G. Pierce, T. D. de la Rubia, Dislocation multi-junctions and strain hardening. *Nature* **440**, 1174–1178 (2006).
2. A. H. Cottrell, B. A. Bilby, Dislocation theory of yielding and strain ageing of iron. *Proc. Phys. Soc. A* **62**, 49–62 (1949).
3. E. Orowan, Zur Kristallplastizität. III. *Zeitschrift für Physik* **89**, 634–659 (1934).
4. W. Bollmann, Interference effects in the electron microscopy of thin crystal foils. *Phys. Rev.* **103**, 1588–1589 (1956).
5. J. Hu, Y. N. Shi, X. Sauvage, G. Sha, K. Lu, Grain boundary stability governs hardening and softening in extremely fine nanograined metals. *Science* **355**, 1292–1296 (2017).
6. M. Legros, G. Dehm, E. Arzt, T. J. Balk, Observation of giant diffusivity along dislocation cores. *Science* **319**, 1646–1649 (2008).
7. S. Lynch, Hydrogen embrittlement phenomena and mechanisms. *Corrosion Rev.* **30**, 105–123 (2012).
8. Y.-S. Chen, D. Haley, S. S. A. Gerstl, A. J. London, F. Sweeney, R. A. Wepf, W. M. Rainforth, P. A. J. Bagot, M. P. Moody, Direct observation of individual hydrogen atoms at trapping sites in a ferritic steel. *Science* **355**, 1196–1199 (2017).
9. Y. S. Chen, H. Lu, J. Liang, A. Rosenthal, H. Liu, G. Sneddon, I. McCarroll, Z. Zhao, W. Li, A. Guo, J. M. Cairney, Observation of hydrogen trapping at dislocations, grain boundaries, and precipitates. *Science* **367**, 171–175 (2020).
10. Y. Yu, C. Zhou, S. Zhang, M. Zhu, M. Wuttig, C. Scheu, D. Raabe, G. J. Snyder, B. Gault, O. Cojocaru-Mirédin, Revealing nano-chemistry at lattice defects in thermoelectric materials using atom probe tomography. *Mater. Today* **32**, 260–274 (2020).
11. Y. Yu, S. Zhang, A. M. Mio, B. Gault, A. Sheskin, C. Scheu, D. Raabe, F. Zu, M. Wuttig, Y. Amouyal, O. Cojocaru-Mirédin, Ag-segregation to dislocations in PbTe-based thermoelectric materials. *ACS Appl. Mater. Inter.* **10**, 3609–3615 (2018).
12. D. Blavette, E. Cadel, A. Fraczkiewicz, A. Menand, Three-dimensional atomic-scale imaging of impurity segregation to line defects. *Science* **286**, 2317–2319 (1999).
13. K. Thompson, P. L. Flaitz, P. Ronsheim, D. J. Larson, T. F. Kelly, Imaging of arsenic Cottrell atmospheres around silicon defects by three-dimensional atom probe tomography. *Science* **317**, 1370–1374 (2007).
14. M. Kuzmina, M. Herbig, D. Ponge, S. Sandlobes, D. Raabe, Linear complexions: Confined chemical and structural states at dislocations. *Science* **349**, 1080–1083 (2015).
15. P. Kontis, Z. Li, D. M. Collins, J. Cormier, D. Raabe, B. Gault, The effect of chromium and cobalt segregation at dislocations on nickel-based superalloys. *Scr. Mater.* **145**, 76–80 (2018).
16. X. X. Wu, S. K. Makineni, C. H. Liebscher, G. Dehm, J. R. Mianroodi, P. Shanthraj, B. Svendsen, D. Bürger, G. Eggeler, D. Raabe, B. Gault, Unveiling the Re effect in Ni-based single crystal superalloys. *Nat. Commun.* **11**, 389 (2020).
17. S. J. Zhou, D. L. Preston, P. S. Lomdahl, D. M. Beazley, Large-scale molecular dynamics simulations of dislocation intersection in copper. *Science* **279**, 1525–1527 (1998).
18. J. Li, S. Sarkar, W. T. Cox, T. J. Lenosky, E. Bitzek, Y. Wang, Diffusive molecular dynamics and its application to nanoindentation and sintering. *Phys. Rev. B* **84**, 054103 (2011).
19. M. Ponga, D. Y. Sun, A unified framework for heat and mass transport at the atomic scale. *Modelling. Simul. Mater. Sci. Eng.* **26**, 035014 (2018).
20. E. Dontsova, J. Rottler, C. W. Sinclair, Solute-defect interactions in Al-Mg alloys from diffusive variational Gaussian calculations. *Phys. Rev. B* **90**, 174102 (2014).
21. V. Turlo, T. J. Rupert, Linear complexions: Metastable phase formation and coexistence at dislocations. *Phys. Rev. Lett.* **122**, 126102 (2019).
22. F. Leonard, M. Haataja, Alloy destabilization by dislocations. *Appl. Phys. Lett.* **86**, 181909 (2005).
23. J. R. Mianroodi, P. Shanthraj, P. Kontis, J. Cormier, B. Gault, B. Svendsen, D. Raabe, Atomistic phase field chemomechanical modeling of dislocation-solute-precipitate interaction in Ni–Al–Co. *Acta Mater.* **175**, 250–261 (2019).
24. D. Hull, D. J. Bacon, *Introduction to Dislocations* (Butterworth-Heinemann, ed. 4, 2001).
25. M. Herbig, D. Raabe, Y. J. Li, P. Choi, S. Zaefferer, S. Goto, Atomic-scale quantification of grain boundary segregation in nanocrystalline material. *Phys. Rev. Lett.* **112**, 126103 (2014).
26. X. Zhou, X.-x. Yu, T. Kaub, R. L. Martens, G. B. Thompson, Grain Boundary Specific Segregation in Nanocrystalline Fe(Cr). *Sci. Rep.* **6**, 34642 (2016).
27. S. K. Makineni, M. Lenz, P. Kontis, Z. Li, A. Kumar, P. J. Felfer, S. Neumeier, M. Herbig, E. Spiecker, D. Raabe, B. Gault, Correlative microscopy—Novel methods and their applications to explore 3D chemistry and structure of nanoscale lattice defects: A case study in superalloys. *JOM* **70**, 1736–1743 (2018).
28. C. J. O'Brien, C. M. Barr, P. M. Price, K. Hattar, S. M. Foiles, Grain boundary phase transformations in PtAu and relevance to thermal stabilization of bulk nanocrystalline metals. *J. Mater. Sci.* **53**, 2911–2927 (2018).
29. Y. Liu, J. Wang, Y. Du, G. Sheng, Z. Long, L. Zhang, Phase boundary migration, Kirkendall marker shift and atomic mobilities in fcc Au–Pt alloys. *Calphad* **36**, 94–99 (2012).
30. F. Kroupa, Dislocation dipoles and dislocation loops. *J. Phys. Colloques* **27**, C3-154–C3-167 (1966).
31. B. Gault, M. P. Moody, F. de Geuser, A. la Fontaine, L. T. Stephenson, D. Haley, S. P. Ringer, Spatial resolution in atom probe tomography. *Microsc. Microanal.* **16**, 99–110 (2010).
32. M. K. Miller, M. G. Hetherington, Local magnification effects in the atom probe. *Surf. Sci.* **246**, 442–449 (1991).
33. F. De Geuser, B. Gault, Metrology of small particles and solute clusters by atom probe tomography. *Acta Mater.* **188**, 406–415 (2020).
34. S. K. Makineni, A. Kumar, M. Lenz, P. Kontis, T. Meiners, C. Zenk, S. Zaefferer, G. Eggeler, S. Neumeier, E. Spiecker, D. Raabe, B. Gault, On the diffusive phase transformation mechanism assisted by extended dislocations during creep of a single crystal CoNi-based superalloy. *Acta Mater.* **155**, 362–371 (2018).
35. G. D. W. Smith, D. Hudson, P. D. Styman, C. A. Williams, Studies of dislocations by field ion microscopy and atom probe tomography. *Philos. Mag.* **93**, 3726–3740 (2013).
36. A. K. da Silva, G. Leyson, M. Kuzmina, D. Ponge, M. Herbig, S. Sandlöbes, B. Gault, J. Neugebauer, D. Raabea, Confined chemical and structural states at dislocations in Fe-9wt%Mn steels: A correlative TEM-atom probe study combined with multiscale modelling. *Acta Mater.* **124**, 305–315 (2017).
37. K. Hoummada, D. Mangelinck, B. Gault, M. Cabie, Nickel segregation on dislocation loops in implanted silicon. *Scr. Mater.* **64**, 378–381 (2011).
38. K. Srivastava, S. I. Rao, J. A. El-Awady, Unveiling the role of super-jogs and dislocation induced atomic-shuffling on controlling plasticity in magnesium. *Acta Mater.* **161**, 182–193 (2018).

39. T. Kadoyoshi, H. Kaburaki, F. Shimizu, H. Kimizuka, S. Jitsukawa, J. Li, Molecular dynamics study on the formation of stacking fault tetrahedra and unfaulting of Frank loops in fcc metals. *Acta Mater.* **55**, 3073–3080 (2007).
40. L. Zhang, C. Lu, G. Michal, G. Deng, K. Tieu, The formation and destruction of stacking fault tetrahedron in fcc metals: A molecular dynamics study. *Scr. Mater.* **136**, 78–82 (2017).
41. J. Silcox, P. B. Hirsch, Direct observations of defects in quenched gold. *Philos. Mag.* **4**, 72–89 (1959).
42. B. N. Singh, D. J. Edwards, P. Toft, Effect of neutron irradiation and post-irradiation annealing on microstructure and mechanical properties of OFHC-copper. *J. Nucl. Mater.* **299**, 205–218 (2001).
43. H. Suzuki, Segregation of solute atoms to stacking faults. *J. Physical Soc. Japan* **17**, 322–325 (1962).
44. J. F. Curry, T. F. Babuska, T. A. Furnish, P. Lu, D. P. Adams, A. B. Kustas, B. L. Nation, M. T. Dugger, M. Chandross, B. G. Clark, B. L. Boyce, C. A. Schuh, N. Argibay, Achieving ultralow wear with stable nanocrystalline metals. *Adv. Mater.* **30**, 1802026 (2018).
45. H. A. Gasteiger, S. S. Kocha, B. Sompalli, F. T. Wagner, Activity benchmarks and requirements for Pt, Pt-alloy, and non-Pt oxygen reduction catalysts for PEMFCs. *Appl. Catal. B Environ.* **56**, 9–35 (2005).
46. O. Kasian, J.-P. Grote, S. Geiger, S. Cherevko, K. J. J. Mayrhofer, The common intermediates of oxygen evolution and dissolution reactions during water electrolysis on iridium. *Angew. Chem. Int. Edit.* **57**, 2488–2491 (2018).
47. X. Song, G. Daniels, D. M. Feldmann, A. Gurevich, D. Larbalestier, Electromagnetic, atomic structure and chemistry changes induced by Ca-doping of low-angle $YBa_2Cu_3O_7$-delta grain boundaries. *Nat. Mater.* **4**, 470–475 (2005).
48. E. F. Rauch, J. Portillo, S. Nicolopoulos, D. Bultreys, S. Rouvinmov, P. Moeck, Automated nanocrystal orientation and phase mapping in the transmission electron microscope on the basis of precession electron diffraction. *Zeitschrift für Kristallographie* **225**, 103–109 (2010).
49. M. Kamaya, M. Kuroda, Fatigue damage evaluation using electron backscatter diffraction. *Mater. Trans.* **52**, 1168–1176 (2011).
50. M. Gallaugher, Y. Ding, P. Ghosh, R. R. Chromik, Local scale microstructural effects from the deformation and recrystallization of non-oriented electrical steels. *Metall. Mater. Trans. E* **3**, 250–263 (2016).
51. V. Turlo, T. J. Rupert, Prediction of a wide variety of linear complexions in face centered cubic alloys. *Acta Mater.* **185**, 129–141 (2020).
52. J. P. Mendez, M. Ponga, MXE: A package for simulating long-term diffusive mass transport phenomena in nanoscale systems. *Comput. Phys. Commun.* **260**, 107315 (2021).
53. S. Plimpton, Fast parallel algorithms for short-range molecular dynamics. *J. Comput. Phys.* **117**, 1–19 (1995).
54. S. Alexander, Visualization and analysis of atomistic simulation data with OVITO–the Open Visualization Tool. *Modelling Simul. Mater. Sci. Eng.* **18**, 015012 (2009).
55. B. Gault, M. P. Moody, F. de Geuser, G. Tsafnat, A. la Fontaine, L. T. Stephenson, D. Haley, S. P. Ringer, Advances in the calibration of atom probe tomographic reconstruction. *J. Appl. Phys.* **105**, 034913 (2009).
56. O. C. Hellman, J. B. du Rivage, D. N. Seidman, Efficient sampling for three-dimensional atom probe microscopy data. *Ultramicroscopy* **95**, 199–205 (2003).
57. H. Okamoto, T. B. Massalski, The Au−Pt (Gold-Platinum) system. *Bull. Alloy Phase Diagrams* **6**, 46–56 (1985).
58. V. Bulatov, W. Cai, *Computer Simulations of Dislocations* (OUP Oxford, 2006).
59. J.-Y. Zhang, W.-Z. Zhang, A general method to construct dislocations in atomistic simulations. *Modelling Simul. Mater. Sci. Eng.* **27**, 035008 (2019).

Acknowledgments: We appreciated the discussion with S. Foiles. J.R.M. acknowledges the fruitful discussions with M. Ponga regarding simulations. **Funding:** X.Z. is supported by Alexander von Humboldt-Stiftung. G.B.T. gratefully acknowledges NSF-DMR-1709803 for support of this work. J.R.M., B.S., and P.S. gratefully acknowledge funding support of DFG through Priority Program 1713. **Author contributions:** D.R. conceived of the presented idea. X.Z. conducted the experiments and analytical characterization. J.R.M. provided simulation results. B.S. and P.S. supervised simulation study. B.G. guided atom probe analysis. T.K. and G.B.T. provided the sample and technical interpretation of experimental findings. G.B.T. and A.K.d.S. gave advice on sample preparation. All authors provided critical feedback and helped shape the research, analysis, and manuscript. **Competing interests:** The authors declare that they have no competing interests. **Data and materials availability:** All data are available in the main text or the Supplementary Materials.

Submitted 1 October 2020
Accepted 1 March 2021
Published 16 April 2021
10.1126/sciadv.abf0563

Citation: X. Zhou, J. R. Mianroodi, A. Kwiatkowski da Silva, T. Koenig, G. B. Thompson, P. Shanthraj, D. Ponge, B. Gault, B. Svendsen, D. Raabe, The hidden structure dependence of the chemical life of dislocations. *Sci. Adv.* **7**, eabf0563 (2021).

Science Advances

The hidden structure dependence of the chemical life of dislocations

X. ZhouJ. R. MianroodiA. Kwiatkowski da SilvaT. KoenigG. B. ThompsonP. ShanthrajD. PongeB. GaultB. SvendsenD. Raabe

Sci. Adv., 7 (16), eabf0563. • DOI: 10.1126/sciadv.abf0563

Science Advances (ISSN 2375-2548) is published by the American Association for the Advancement of Science. 1200 New York Avenue NW, Washington, DC 20005. The title *Science Advances* is a registered trademark of AAAS.